

# SUNYAEV–ZEL'DOVICH EFFECT OBSERVATIONS OF THE BULLET CLUSTER (1E 0657–56) WITH APEX-SZ

N. W. HALVERSON<sup>1,2</sup>, T. LANTING<sup>3</sup>, P. A. R. ADE<sup>4</sup>, K. BASU<sup>5</sup>, A. N. BENDER<sup>1</sup>, B. A. BENSON<sup>6</sup>, F. BERTOLDI<sup>5</sup>, H.-M. CHO<sup>7</sup>,  
 G. CHON<sup>8</sup>, J. CLARKE<sup>6,9</sup>, M. DOBBS<sup>3</sup>, D. FERRUSCA<sup>6</sup>, R. GÜSTEN<sup>8</sup>, W. L. HOLZAPFEL<sup>6</sup>, A. KOVÁCS<sup>8</sup>, J. KENNEDY<sup>3</sup>, Z. KERMISH<sup>6</sup>,  
 R. KNESSL<sup>8</sup>, A. T. LEE<sup>6,9</sup>, M. LUEKER<sup>6</sup>, J. MEHL<sup>6</sup>, K. M. MENTEN<sup>8</sup>, D. MUDERS<sup>8</sup>, M. NORD<sup>5,8</sup>, F. PACAUD<sup>5</sup>, T. PLAGGE<sup>6</sup>,  
 C. REICHARDT<sup>6</sup>, P. L. RICHARDS<sup>6</sup>, R. SCHAAF<sup>5</sup>, P. SCHILKE<sup>8</sup>, F. SCHULLER<sup>8</sup>, D. SCHWAN<sup>6</sup>, H. SPIELER<sup>9</sup>, C. TUCKER<sup>4</sup>, A. WEISS<sup>8</sup>,  
 AND O. ZAHN<sup>6</sup>

<sup>1</sup> Center for Astrophysics and Space Astronomy, Department of Astrophysical and Planetary Sciences, University of Colorado, Boulder, CO 80309, USA

<sup>2</sup> Department of Physics, University of Colorado, Boulder, CO 80309, USA

<sup>3</sup> Department of Physics, McGill University, Montréal H3A 2T8, Canada

<sup>4</sup> School of Physics and Astronomy, Cardiff University, CF24 3YB Wales, UK

<sup>5</sup> Argelander Institute for Astronomy, Bonn University, Bonn, Germany

<sup>6</sup> Department of Physics, University of California, Berkeley, CA 94720, USA

<sup>7</sup> National Institute of Standards and Technology, Boulder, CO 80305, USA

<sup>8</sup> Max Planck Institute for Radioastronomy, 53121 Bonn, Germany

<sup>9</sup> Lawrence Berkeley National Laboratory, Berkeley, CA 94720, USA

Received 2008 July 25; accepted 2009 June 8; published 2009 July 20

## ABSTRACT

We present observations of the Sunyaev–Zel’dovich effect (SZE) in the Bullet cluster (1E 0657–56) using the APEX-SZ instrument at 150 GHz with a resolution of 1′. The main results are maps of the SZE in this massive, merging galaxy cluster. The cluster is detected with 23 $\sigma$  significance within the central 1′ radius of the source position. The SZE map has a broadly similar morphology to that in existing X-ray maps of this system, and we find no evidence for significant contamination of the SZE emission by radio or IR sources. In order to make simple quantitative comparisons with cluster gas models derived from X-ray observations, we fit our data to an isothermal elliptical  $\beta$  model, despite the inadequacy of such a model for this complex merging system. With an X-ray-derived prior on the power-law index,  $\beta = 1.04^{+0.16}_{-0.10}$ , we find a core radius  $r_c = 142'' \pm 18''$ , an axial ratio of  $0.889 \pm 0.072$ , and a central temperature decrement of  $-771 \pm 71 \mu\text{K}_{\text{CMB}}$ , including a  $\pm 5.5\%$  flux calibration uncertainty. Combining the APEX-SZ map with a map of projected electron surface density from *Chandra* X-ray observations, we determine the mass-weighted temperature of the cluster gas to be  $T_{\text{mg}} = 10.8 \pm 0.9 \text{ keV}$ , significantly lower than some previously reported X-ray spectroscopic temperatures. Under the assumption of an isothermal cluster gas distribution in hydrostatic equilibrium, we compute the gas mass fraction for prolate and oblate spheroidal geometries and find it to be consistent with previous results from X-ray and weak-lensing observations. This work is the first result from the APEX-SZ experiment, and represents the first reported scientific result from observations with a large array of multiplexed superconducting transition-edge sensor bolometers.

**Key words:** cosmic microwave background – cosmology: observations – galaxies: clusters: individual (1E 0657–56)

*Online-only material:* color figures

## 1. INTRODUCTION

Clusters of galaxies are a unique probe of the growth and dynamics of structure in the universe. In particular, active mergers of subclusters provide a window to the processes by which massive clusters are assembled. In these systems, the galaxies and associated dark matter are essentially collisionless. In contrast, the ionized intracluster gas, typically at temperatures of  $T \sim 10^8 \text{ K}$ , is strongly interacting and experiences complex dynamics. In extreme cases, the normally associated dark matter and intracluster gas can be significantly separated.

The Bullet cluster (1E 0657–56) at  $z = 0.296$ , is a massive cluster consisting of two subclusters in the process of merging. The smaller subcluster or “bullet” has passed through the larger main cluster. X-ray observations infer a bow shock velocity of  $\sim 4700 \text{ km s}^{-1}$  (Markevitch 2006), while simulations of the collision yield a substantially lower speed for the subcluster (Springel & Farrar 2007). This collision is perpendicular to the line of sight, providing an ideal system for studying interacting subclusters (Clowe et al. 2006).

The mass surface density of the Bullet cluster has been measured using weak and strong gravitational lensing of light from background galaxies. There are significant angular offsets between the peaks of the X-ray surface brightness, which trace the baryonic gas through thermal bremsstrahlung emission, and the peaks of the lensing surface density, which are associated with the majority of the mass. The combined weak- and strong-lensing analyses of Bradač et al. (2006) show that the main cluster and subcluster are separated from their associated X-ray peaks at  $10\sigma$  and  $6\sigma$  significance, respectively. This result has been recognized as providing direct evidence for the presence of collisionless dark matter in this system (Clowe et al. 2006).

The Sunyaev–Zel’dovich effect (SZE) provides an independent probe of the intracluster gas. In the SZE, a small fraction ( $\sim 1\%$ ) of cosmic microwave background (CMB) photons undergo inverse Compton scattering from intracluster electrons (Sunyaev & Zel’dovich 1970; Birkinshaw 1999). This process distorts the Planck blackbody spectrum of the CMB and produces a signal proportional to the gas pressure integrated along the line of sight. At 150 GHz, the SZE produces a temperature decrement with respect to the unperturbed CMB intensity.

Early detections of the SZE in the Bullet cluster include work by Andreani et al. (1999) and Gomez et al. (2004).

Unlike the X-ray surface brightness, the peak SZE surface brightness for a given cluster is independent of redshift. Therefore, the SZE has the potential to be an effective probe of intra-cluster gas out to the redshifts at which clusters are assembled. SZE measurements of galaxy clusters provide complementary constraints on cluster properties typically derived from X-ray measurements such as central electron density, core radius of the intracluster gas, cluster gas mass, and fraction of the total cluster mass in gas. Since the SZE and X-ray signals are proportional to the line-of-sight integral of the electron density and electron density squared, respectively, SZE results will be less sensitive to clumping of the intracluster gas. For all comparisons between SZ and X-ray data, we assume a  $\Lambda$ CDM cosmology, with  $h = 0.7$ ,  $\Omega_m = 0.27$ , and  $\Omega_\Lambda = 0.73$ .

In this paper, we present a  $1'$  resolution SZE image of the Bullet cluster at 150 GHz made with the APEX-SZ instrument. It is the first reported scientific result from observations with a large array of multiplexed superconducting transition-edge sensor bolometers. In Section 2, we discuss the instrument and observations. Calibration is discussed in Section 3. In Section 4, we describe the data reduction procedure; and in Section 5, we present the results of fits to the SZE surface brightness with cluster models, including mass-weighted electron temperature and gas mass fraction calculations. We summarize the conclusions and discuss future work in Section 6.

## 2. OBSERVATIONS

APEX-SZ is a receiver designed specifically for SZE galaxy cluster surveys (Schwan et al. 2003; Dobbs et al. 2006; D. Schwan et al. 2009, in preparation). It is mounted on the 12 m diameter APEX telescope, located on the Atacama plateau in northern Chile (Güsten et al. 2006). The observing site was chosen for its extremely dry and stable atmospheric conditions. The mean atmospheric transmittance is frequently better than 95% in the APEX-SZ frequency band at 150 GHz (Peterson et al. 2003; Chamberlain & Bally 1995). The telescope is capable of round-the-clock observations.

Three reimaging mirrors in the Cassegrain cabin couple the APEX telescope to the focal plane of APEX-SZ. We achieve the diffraction-limited performance of the telescope across the entire  $0.4'$  field of view (FOV) with a mean measured beam full width at half-maximum (FWHM) of  $58''$ , and a measured beam solid angle of  $1.5 \text{ arcmin}^2$ , including measured sidelobes at the  $-14 \text{ dB}$  level.

The APEX-SZ receiver houses a cryogenic focal plane, operating at 0.3 K. The focal plane contains 330 horn-fed absorber-coupled superconducting transition-edge sensor bolometers (Richards 1994; Lee et al. 1996), with 55 detectors on each of the six subarray wafers. Of the 330 detectors, 280 are read out with the current frequency-domain multiplexed readout hardware. We measure the median individual pixel noise-equivalent power (NEP) to be  $10^{-16} \text{ W}/\sqrt{\text{Hz}}$  and the median noise equivalent temperature (NET) to be  $860 \mu\text{K}_{\text{CMB}}\sqrt{\text{s}}$ . The measured optical bandwidth of the receiver is 40% narrower than the design goal of 38 GHz, resulting in lower sensitivity than anticipated.

The large FOV of the APEX-SZ instrument is designed for surveying large areas of sky. In order to efficiently observe a single target, we use the circular scan pattern illustrated in Figure 1. The circle center is fixed in AZ/EL coordinates for 20 circular subscans, with a total duration of 100 s. This choice has

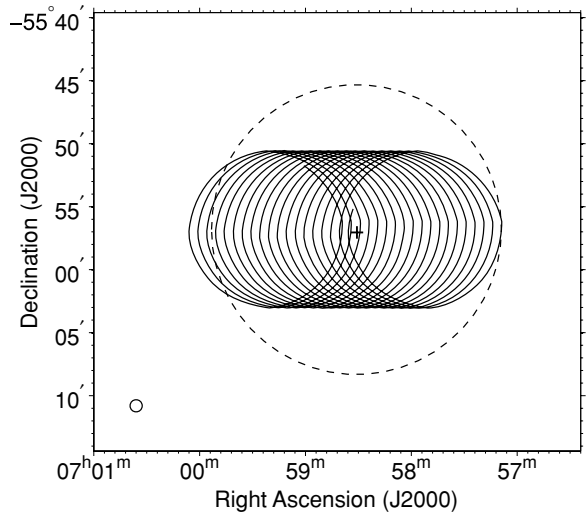


**Figure 1.** 100 s circular drift scan pattern. The solid line shows the track of the center of the array. One circle has a period of 5 s. The dashed line shows the instantaneous FOV of the bolometer array. The + marker indicates the source position with respect to the scan pattern. The center of the circles is constant in azimuth and elevation as the source drifts across the field. The small disk in the lower left indicates the  $58''$  mean FWHM beam for a single bolometer.

a number of important advantages. The sky signal is modulated so that it appears in the timestream at frequencies higher than atmospheric drifts and readout  $1/f$  noise. In addition, the circle scan has a moderate continuous acceleration; the lack of high-acceleration turnarounds makes it possible to achieve a high observing efficiency. Approximately 20% of the total observing time is spent moving the telescope to a new center position before the start of the next scan. Every bolometer maps a  $12' \times 25'$  subfield, with a combined map field of  $36' \times 48'$  every 100 s.

Observations of the Bullet cluster were conducted over a period of 7 days in 2007 August, when the cluster was visible between the hours of 03:00 and 15:00 local time. The weather over this period was typical for the site, with precipitable water vapor varying between 0.25 and 1.5 mm, and a median atmospheric transmittance of 97%. For the analysis in this paper, 235 scans are used, each scan consisting of twenty 5 s circular subscans, for a total of 6.4 hr of on-source data.

## 3. CALIBRATION

The response of the receiver to astronomical sources is measured with daily raster scans of Mars over every bolometer in the array. For each bolometer, the observations provide a primary flux calibration and a high signal-to-noise beam profile from which we determine beam parameters such as size, ellipticity, and position with respect to the array-center pointing. Additional observations of RCW57 and RCW38 are used to monitor gain stability, and frequent observations of bright quasars near the cluster source are used to monitor pointing stability.

The WMAP satellite has been used to calibrate the brightness temperature of Mars at 93 GHz in five measurement periods spanning several years (Hill et al. 2009). The WMAP Mars temperatures are tied to the CMB dipole moment and are accurate to better than 1.0%. The brightness temperature of Mars changes significantly ( $\sim 15\%$ ) as a function of its orbit and orientation. We use a version of the Rudy model (Rudy et al. 1987; Muhleman & Berge 1991), that has been updated

and maintained by Bryan Butler,<sup>10</sup> to transfer the *WMAP* Mars temperature results to the APEX-SZ frequency band and specific times of our Mars observations.

After applying a constant scaling factor, we find the Rudy model predictions for the Mars brightness temperature to be in excellent agreement with the *WMAP* measurements. We find that the Rudy model brightness temperatures at 93 GHz are systematically a factor of  $1.052 \pm 0.010$  higher than those measured by *WMAP* in the five published observation periods. In contrast, repeating the same exercise with the thermal model developed by Wright (1976, 2007), as implemented in the online JCMT-FLUXES program,<sup>11</sup> results in a scaling factor of  $1.085 \pm 0.043$ . This is consistent with the 10% rescaling of this model called for in Hill et al. (2009), but the scaling factor exhibits significantly larger rms scatter than that of the Rudy model.

We therefore use the *WMAP* 93 GHz calibrated Rudy model to compute the Mars brightness temperatures at 150 GHz for the specific times of our Mars observations by reducing the Rudy model 150 GHz temperatures by a factor of 1.052. The Rudy model 150/93 GHz frequency scaling factor is  $1.016 \pm 0.009$  at the times of our Mars observations, and we adopt the rms scatter in this frequency scaling factor as an estimate of its uncertainty. Combining the uncertainties in the *WMAP* Mars calibration, the *WMAP* to Rudy model scaling factor at 93 GHz, and the Rudy model frequency scaling factor, we estimate the uncertainty in Mars temperature to be  $\pm 1.7\%$ .

The measured signals from the calibrators are corrected for atmospheric opacity, which is measured with a sky dip observation at the beginning and end of each day's observations. Measured zenith transmittance over the observing period ranged between 0.92 and 0.98, with a median of 0.97. Based on the observed temporal variability of the opacity, drifts in atmospheric opacity between the sky dip and observation contribute  $< 0.4\%$  to the overall calibration uncertainty. After correcting for the atmospheric opacity, we find that the Mars temperature measured by APEX-SZ varies from the model prediction by up to  $\sim 3\%$  over the course of the observation period. This gain variation is included as a source of error in the final calibration uncertainty. The APEX-SZ observing band center is measured with a Fourier transform spectrometer to be  $152 \pm 2$  GHz. The uncertainty in the band center results in a  $\pm 1.4\%$  uncertainty in extrapolation of the Mars-based calibration to CMB temperature.

The beam shape, including near sidelobes, is characterized by creating a beam map from Mars observations, combining the same bolometer channels that are used to make the science maps. We adjust the calibration and measured beam size for the small ( $\sim 1\%$ ) correction due to the  $8''$  angular size of Mars. We estimate a fractional uncertainty in the beam solid angle of  $\pm 4\%$ .

The APEX-SZ detectors operate in a state of strong negative electrothermal feedback, which results in a linear response to changes in the input optical power. We have measured the response of the detectors during sky dips between  $90^\circ$  and  $30^\circ$  elevation (antenna temperature difference  $\sim 13$  K), and find no significant deviation from the expected linear response to loading. We therefore conclude that detector nonlinearity makes a negligible contribution to the calibration uncertainty.

Slowly changing errors in telescope pointing result in both a pointing uncertainty and a flux calibration uncertainty due a

**Table 1**  
APEX-SZ Flux Calibration Uncertainty

Source	Uncertainty
<i>WMAP</i> Mars temperature at 93 GHz	$\pm 1.0\%$
Rudy model to <i>WMAP</i> scaling factor at 93 GHz	$\pm 1.0\%$
150/93 GHz frequency scaling factor	$\pm 0.9\%$
Frequency band center	$\pm 1.4\%$
Beam solid angle	$\pm 4.0\%$
Atmospheric attenuation	$\pm 0.4\%$
Gain variation	$\pm 3.0\%$
Total	$\pm 5.5\%$

broadening of the effective beam pattern. To measure pointing errors during our observations, we observe a bright quasar within a few degrees of the Bullet cluster every 1–2 hr, and apply a pointing correction as needed. The typical rms pointing variations of the APEX telescope between quasar observations are  $\sim 4''$ . This pointing uncertainty results in a slightly larger effective beam for the co-added maps than is measured with the individual calibrator maps. The correction to the flux calibration of the co-added maps due to pointing uncertainty is negligible, particularly for the observation of extended objects such as the Bullet cluster. We estimate the pointing uncertainty in the co-added maps to be  $\pm 4''$  in both the R.A. and decl. directions.

The uncertainty in the CMB temperature calibration of the APEX-SZ maps is summarized in Table 1. The combination of all contributions to the calibration uncertainty described above results in an overall point-source flux uncertainty of  $\pm 5.5\%$ .

#### 4. DATA REDUCTION

The data consist of 280 bolometer timestreams sampled at 100 Hz, telescope pointing data interpolated to the same rate, housekeeping thermometry data, bolometer bias and readout configuration data, and other miscellaneous monitoring data. The fundamental observation unit is a scan comprising twenty 5 s circular subscans in AZ/EL coordinates, allowing the source to drift through the FOV, as described in Section 2 above.

Data reduction consists of cuts to remove poor-quality data, filtering of  $1/f$  and correlated noise due to atmospheric fluctuations, and binning the bolometer data into maps. These steps are described in more detail below.

##### 4.1. Timestream Data Cuts

Timestream data are first parsed into individual circular subscans. We reject  $\sim 7\%$  of the data at the beginning and end of the scan where the telescope deviates from the constant angular velocity circular pattern. We reject bolometer channels that are optically or electronically unresponsive, or lack high-quality flux calibration data; typically, 160–200 of the 280 bolometer channels remain after these preliminary cuts. The large number of rejected channels is primarily due to low fabrication yield for two of the six bolometer subarray wafers.

We reject spikes and step-like glitches caused by cosmic rays or electrical interference. These are infrequent and occur on timescales faster than the detector optical time constant. We use a simple signal-to-noise cut on the data to reject these, since the timestream is noise dominated even for the  $\sim 1$  mK Bullet cluster signal. Step-like glitches are often correlated across many channels in the array, so we reject data from all channels

<sup>10</sup> <http://www.aoc.nrao.edu/~bbutler/work/mars/model/>

<sup>11</sup> <http://www.jach.hawaii.edu/jac-bin/planetflux.pl>



whenever a spike or glitch in  $\geq 2\%$  of the channels is detected. These cuts result in a loss of 8% of the remaining data.

For each circular subscan, we also reject channels that have excessive noise in signal band, resulting in a loss of 19% of the remaining data.

#### 4.2. Atmospheric Fluctuation Removal

After the timestream data cuts, fluctuations in atmospheric emission produce the dominant signal in the raw bolometer timestreams. The atmospheric signal is highly correlated across the array, which can be exploited to remove the signal. Principal component analysis (PCA) has been used by some groups to reduce the atmospheric signal (see, e.g., Scott et al. 2008; Laurent et al. 2005). However, the effect of PCA filtering on the source is difficult to predict and is a function of the atmospheric conditions. We have developed an analysis strategy that reduces the atmospheric signal through the application of spatial filters that have a constant and well understood effect on the signals we are attempting to measure.

Atmospheric fluctuation power is expected to follow a Kolmogorov spatial power spectrum, with most power present on scales larger than the separation between beams as they pass through the atmosphere, resulting in an atmospheric signal that is highly correlated across the array. To reduce these fluctuations, we first remove a polynomial and an elevation-dependent air mass opacity model from each channel's timestream, then remove a first-order two-dimensional spatial polynomial across the array for each time step. This algorithm is described in detail in the two following subsections. This atmospheric fluctuation removal strategy requires that both the spatial extent of the scan pattern and the instantaneous array FOV are larger than the source. The 6' radius circular scan and the 23' array FOV allow us to recover most of the Bullet cluster's flux, but some extended emission is lost as is described in Section 5.

##### 4.2.1. Timestream Atmosphere Removal

We observe scan-synchronous signals in the bolometer timestreams due to elevation-dependent atmospheric emission. The optical path length  $L$  through the atmosphere is proportional to the cosecant of the elevation angle  $\epsilon$ ,  $L \propto \csc(\epsilon)$ . The change in optical path length is nearly a linear function of elevation angle over the 6' circular scan radius. In the circular drift scans, this modulation of the elevation-dependent opacity produces an approximately sinusoidal modulation in the bolometer timestream. For each channel in each scan, we simultaneously fit and remove an atmospheric model consisting of this cosecant function plus an order 20 polynomial (1 degree of freedom per circular subscan) to remove slow drifts in the atmospheric opacity and readout  $1/f$  noise. This scheme effectively removes the common scan-induced atmospheric signal as well as most of the atmospheric fluctuation power below the frequency of the circular subscan (0.20 Hz), while only modestly affecting the central Bullet cluster signal.

##### 4.2.2. Spatially Correlated Atmosphere Removal

Removing the cosecant-plus-polynomial model from the timestream data reduces low-frequency atmospheric fluctuation power, but not higher frequency power corresponding to smaller spatial scales near those where the cluster signal occurs. To reduce these fluctuations, the atmosphere can be modeled as a spatially correlated signal across the array pixel positions on the sky with a low-order two-dimensional polynomial function. At

each time step, we fit and remove a low-order two-dimensional polynomial function across the array, similar to the procedure described in Sayers (2007). The relative gain coefficients for each bolometer channel are calculated by taking the ratio of each channel's timestream, which is dominated by correlated atmospheric noise, to a median timestream signal generated from all channels. With the favorable atmospheric conditions of these observations, we find that a first-order spatial polynomial (offset and tilt) is adequate to remove most of the atmospheric signal while preserving the cluster signal.

Bolometer channels with excess uncorrelated noise are more easily identified after removing the correlated atmospheric noise component; we reject these noisy channels, then perform the spatially correlated signal removal a second time.

#### 4.3. Map-Making

The atmospheric removal algorithms described above act as a high-pass filter. They suppress signals on scales comparable to the scan length or the focal plane FOV. The cluster emission can be quite extended, and therefore the data reduction filtering process attenuates diffuse flux in the cluster signal and produces small positive sidelobes around the cluster decrement. The data reduction pipeline filters can be tailored, within limits, to meet various scientific objectives. Thus, our primary data products consist of two different high signal-to-noise maps of the cluster.

For one map, we mask a circular region centered on the cluster source prior to fitting the timestream and spatial filters described in Section 4.2, then apply the resulting filter functions to the entire data set, including the source region. The source-mask procedure prevents the cluster signal within the masked region from influencing the baseline fits, and thus reduces attenuation of the source central decrement and extended emission at the expense of increasing the contribution of low-frequency noise in the map center. We choose a source-mask radius of 4.75 as a compromise between attenuation of diffuse emission and increased map noise. We use the source-masked map to visually interpret the morphology and extended emission in the cluster. These results are discussed in Section 5.1.

We also produce a map in which we do not mask the source when applying filters. The non-source-masked map is used for model parameter estimation because it has higher signal-to-noise in the central region of the map. In addition, it is easier to take into account the effects of the data reduction filters, or transfer function, on the underlying sky intensity distribution, which is necessary for comparing the data to the model for parameter estimation. The fitting procedure and results are described in more detail in Section 5.2.

For each of the two maps, the post-cut, filtered timestream data are binned in angular sky coordinates to create maps. For a given scan, a map is created from each bolometer channel, applying the channel's pointing offset and flux calibration. A co-added scan map is created by combining individual channel maps with minimum variance weighting in each pixel, using the sample variance of the conditioned timestream data in the scan. The final co-added map is created by combining all scan maps, again with minimum variance weighting in each pixel. We bin maps at a resolution of 10'' to oversample the beam. The source-masked map that we present in Section 5 is convolved with a 1' FWHM Gaussian to smooth noise fluctuations to the angular size of the beam. However, the radial profiles presented below and the non-source-masked map used for model fitting do not include this additional smoothing.

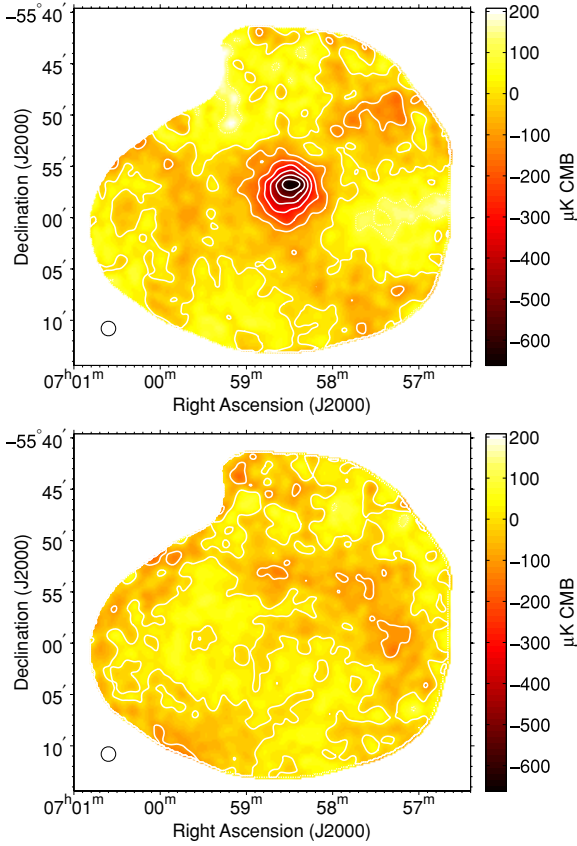


**Figure 2.** Top: temperature map of the Bullet cluster system from the source-masked data reduction, with scale in CMB temperature units. The circle in the lower left corner represents the 85'' FWHM map resolution which is the result of the instrument beam and data reduction filter convolved with the 1' FWHM Gaussian smoothing applied to the map. Bottom: difference map made by multiplying alternate scan maps by +1 and -1, respectively, then co-adding all scan maps with minimum variance weighting, in the same manner as was used to produce the temperature map shown in the top panel. The contour interval is 100  $\mu\text{K}_{\text{CMB}}$  in both maps.

(A color version of this figure is available in the online journal.)

## 5. RESULTS

### 5.1. Temperature Map

Figures 2 and 3 show the source-masked temperature map from our observations of the Bullet cluster. The map has a resolution of 85'' FWHM which results from the combination of the 58'' instrumental beam, the data reduction filters, and a final 1' FWHM Gaussian smoothing of the map. The source-masked map is shown in order to provide a more accurate representation of the extended emission and cluster morphology. The noise in the central region of the source-masked map is 55  $\mu\text{K}_{\text{rms}}$  per 85'' FWHM resolution element. Near the cluster center, the emission hints at elongation in the east–west direction, which is along the axis between the main- and subcluster gas detected in the X-ray, see Section 5.4. The more extended emission appears to be elongated in the northwest–southeast direction, which is the major axis of the best-fit elliptical  $\beta$  model discussed in Section 5.2. Figure 3 shows the centroid position of the best-fit elliptical  $\beta$  model, and the position of the dust obscured, lensed galaxy detected at 270 GHz by Wilson et al. (2008). As discussed in Section 5.3, we see no evidence for emission from this source in our 150 GHz map.

Radial profiles for the unsmoothed source-masked and non-source-masked maps are shown in Figure 4. The source-masked

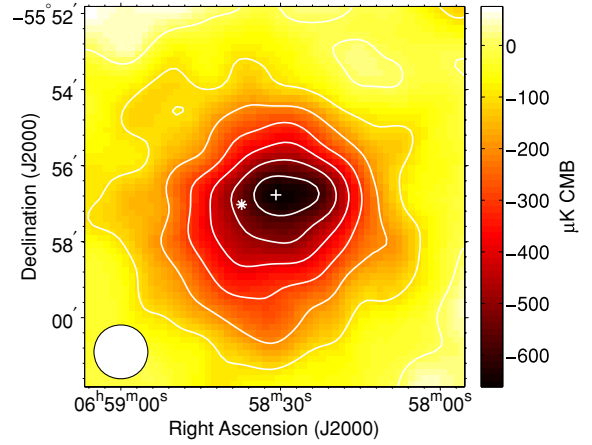


**Figure 3.** Temperature map detail from Figure 2, with color scale adjusted to the limits of the detail region, and a contour interval of 100  $\mu\text{K}_{\text{CMB}}$ . The + marker indicates the centroid position of the best-fit elliptical  $\beta$  model, see Section 5.2. The \* marker indicates the position of the bright, dust obscured, lensed galaxy detected at 270 GHz by Wilson et al. (2008), see Section 5.3.

(A color version of this figure is available in the online journal.)

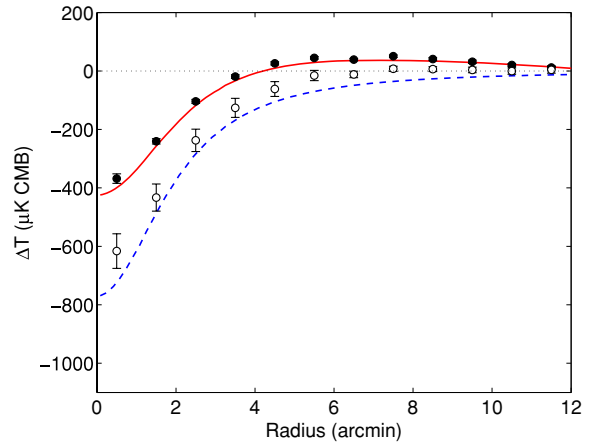


**Figure 4.** Radial profile of the SZE in the Bullet cluster compared to the best-fit  $\beta$  model. Points with error bars are the SZE data binned in 1' radial bins, from the non-source-masked map, ( $\mathcal{M}$ , filled circles) and the source-masked map (open circles). The lines show the radial profile of the best-fit  $\beta$  model, unfiltered ( $\mathcal{B}$ , blue-dashed line) and after convolving with the instrument beam and non-source-masked data reduction filters ( $\mathcal{B}'$ , red solid line). The non-source-masked map radial profile is reasonably well fit by the filtered  $\beta$  model. The source-masked map preserves signal on larger spatial scales than the non-source-masked map, but still attenuates signal on scales exceeding the 4/75 radius of the source masking. The source-masked data thus have a lower signal amplitude when compared with the unfiltered  $\beta$  model, as expected. See the text for details.

(A color version of this figure is available in the online journal.)

map has a signal-to-noise of 10 within the central 1' radius, compared to 23 for the non-source-masked map, due to the fact that source-masking allows more large-scale atmospheric fluctuation noise to remain in the map. However, the source-masked map preserves signal on larger spatial scales than the non-source-masked map. In both the source-masked and non-source-masked maps, the sky intensity distribution is filtered by the instrument beam and data reduction pipeline described in Section 4. We do not renormalize the map amplitudes, since the source is extended and an assumption would need to be made about the shape of the sky-brightness distribution to do so. However, in order to accurately estimate cluster parameters such as the central temperature decrement, a model for cluster

emission must be adopted, and the instrument beam and data reduction filtering must be taken into account.

### 5.2. Fit to Elliptical $\beta$ Model

We fit an elliptical  $\beta$  model to the non-source-masked temperature map to allow a straightforward comparison of cluster gas properties derived from our measurements to those derived from X-ray observations. In all analyses, here, we assume the cluster gas is well described by an isothermal  $\beta$  model, and is in hydrostatic equilibrium. These assumptions are unphysical in the case of the Bullet cluster, which is a dynamically complex merging system where the gas is separated from the rest of the mass (Clowe et al. 2006). However, we find that with the sensitivity and spatial resolution of the observations, these assumptions yield an adequate description of the observed emission.

We model the three-dimensional radial profile of the electron density with an isothermal  $\beta$  model (Cavaliere & Fusco-Femiano 1978):

$$n_e(r) = n_{e0} \left( 1 + \frac{r^2}{r_c^2} \right)^{-3\beta/2}. \quad (1)$$

Here,  $n_{e0}$  is the central electron number density,  $r_c$  is the core radius of the gas distribution, and  $\beta$  describes the power-law index at large radii.

The radial surface temperature profile of the SZE takes a simple analytic form:

$$\Delta T_{\text{SZ}} = \Delta T_0 \left( 1 + \frac{\theta^2}{\theta_c^2} \right)^{(1-3\beta)/2}, \quad (2)$$

where  $\Delta T_0$  is the central temperature decrement, and  $\theta_c = r_c/D_A$  is the core radius divided by the angular-diameter distance. A similar form exists for the X-ray surface brightness.

Because of the significant ellipticity in the measured SZE intensity profile, we generalize the cluster gas model to be a spheroidal rather than a spherical function of the spatial coordinates:

$$\Delta T_{\text{SZ}} = \Delta T_0 (1 + A + B)^{(1-3\beta)/2}, \quad (3)$$

with

$$A = \frac{(\cos(\Phi)(X - X_0) + \sin(\Phi)(Y - Y_0))^2}{\theta_c^2},$$

$$B = \frac{(-\sin(\Phi)(X - X_0) + \cos(\Phi)(Y - Y_0))^2}{(\eta\theta_c)^2}.$$

Here,  $(X - X_0)$  and  $(Y - Y_0)$  are angular offsets on the sky in the R.A. and decl. directions, with respect to center positions  $X_0$  and  $Y_0$ . The axial ratio,  $\eta$ , is the ratio between the minor and major axis core radii,  $\Phi$  is the angle between the major axis and the R.A. ( $X$ ) direction.  $\Delta T_0$  is given by the gas pressure integrated along the central line of sight through the cluster:

$$\frac{\Delta T_0}{T_{\text{CMB}}} = \frac{k_B \sigma_T}{m_e c^2} \int f(x, T_e) n_e(l) T_e(l) dl, \quad (4)$$

where  $x = h\nu/kT$ ,  $f(x, T_e)$  describes the frequency dependence of the SZE,  $\sigma_T$  is the Thomson scattering cross section, and  $T_{\text{CMB}} = 2.728$  K. For all results in this paper, we use the relativistic SZE spectrum  $f(x, T_e)$  provided by Nozawa

et al. (2000), and neglect the kinematic effect. At 150 GHz and  $T_e = 13.9$  keV (see Section 5.4), this is a 9% correction to the nonrelativistic value.

To accurately estimate  $\beta$  model parameters for the cluster, the instrument beam and data reduction filters, or transfer function, must be applied to the model before comparing it with the data (see, e.g., Benson et al. 2003; Reese et al. 2000). We characterize this transfer function by creating a map from a simulated point source, convolved with the instrument beam, and inserted into a noiseless timestream, similar to the method described in Scott et al. (2008). The point-source transfer function map  $\mathcal{K}$  is then convolved with a simulated  $\beta$  model cluster map  $\mathcal{B}$  to generate a filtered model map  $\mathcal{B}'$ , which is a noiseless simulated APEX-SZ observation of a  $\beta$  model cluster. The filtered model map,  $\mathcal{B}'$ , is then differenced with the data map,  $\mathcal{M}$ , and model parameters are estimated by minimizing a  $\chi^2$  statistic.

Simulating maps of many different cluster models is required for model parameter fitting. Convolving the cluster model with the point-source transfer function map is much faster than processing each model through the reduction pipeline. We find that the resulting simulated maps from both methods agree sufficiently well to have negligible effect on the parameter estimation results.

We use the unsmoothed non-source-masked map with  $10''$  pixelization described in Section 4.3 for all parameter estimation described below, since this map has lower noise and a more easily characterized transfer function than the source-masked map shown in Figure 2. Diffuse cluster emission is more attenuated in the non-source-masked map, but this is taken into account using the point-source transfer function.

Map noise properties are assessed in the spatial frequency domain using jackknife noise maps (see Sayers 2007; Sayers et al. 2009). To estimate the noise covariance  $C_n$ , we assume that the noise is stationary in the map basis. With this assumption, the Fourier transform of the noise covariance matrix,  $\tilde{C}_n$ , is diagonal, and the diagonal elements are equal to the noise map power spectral density (PSD). For each of 500 jackknife noise map realizations, we find the two-dimensional Fourier transform, then average over all realizations. This averaged map PSD is the experimental estimate of the diagonal elements of  $\tilde{C}_n$ . However, these jackknife maps do not include fluctuations due to the primary CMB anisotropies. We estimate the CMB signal covariance from the *WMAP5* best-fit power spectrum (Nolta et al. 2009) convolved with the point-source transfer function described earlier and add it to the jackknife noise PSD to determine the total covariance matrix.

We construct a  $\chi^2$  statistic for the model fit using the transform of the filtered  $\beta$  model,  $\tilde{\mathcal{B}}'$ , and the transform of the central  $14' \times 14'$  portion of the data map  $\tilde{\mathcal{M}}$  as

$$\chi^2 = (\tilde{\mathcal{M}} - \tilde{\mathcal{B}}')^T \tilde{C}_n^{-1} (\tilde{\mathcal{M}} - \tilde{\mathcal{B}}'). \quad (5)$$

Using Markov Chain Monte Carlo (MCMC) methods, the likelihood,  $\mathcal{L} = e^{-\frac{1}{2}\chi^2}$ , is sampled in the seven-dimensional model parameter space and integrated to find the marginal likelihood distributions of the  $\beta$  model parameters. The model parameter estimates and uncertainties that we report are the maximum likelihood values and constant-likelihood 68% confidence intervals, respectively, of the marginal likelihood distributions.

The above approach to noise covariance estimation is chosen for its simplicity and because we do not have enough linear combinations of individual scan maps to fully sample the noise covariance matrix using jackknife noise maps. But, the method relies on several simplifying assumptions, including that the



**Table 2**  
 $\beta$  Model Fit Results

Parameter	Description	Value	Uncertainty <sup>a</sup>
$X_0$	R.A. centroid position	06 <sup>h</sup> 58 <sup>m</sup> 30 <sup>s</sup> .86 (J2000)	$\pm 7''.4$
$Y_0$	Decl. centroid position	$-55^\circ 56' 46''.2$ (J2000)	$\pm 7''.3$
$\Delta T_0$	Central temperature decrement	$-771 \mu\text{K}_{\text{CMB}}$	$\pm 71 \mu\text{K}_{\text{CMB}}$
$y_0$	Central Comptonization <sup>b</sup> ( $T_e = 13.9$ keV)	$3.31 \times 10^{-4}$	$\pm 0.30 \times 10^{-4}$
$y_0$	Central Comptonization <sup>b</sup> ( $T_e = 10.6$ keV)	$3.24 \times 10^{-4}$	$\pm 0.30 \times 10^{-4}$
$\theta_c$	Core radius	142''	$\pm 18''$
$\eta$	Ellipse minor/major core radius ratio	0.889	$\pm 0.072$
$\Phi$	Ellipse orientation angle	$-52^\circ$	$\pm 20^\circ$
$\beta$	Power-law index	1.15	$\pm 0.13$

**Notes.**

<sup>a</sup> Quoted uncertainties are 68% confidence intervals in the marginal likelihood distribution for each parameter. The uncertainty in  $\Delta T_0$  includes a statistical uncertainty from the fit of  $\pm 57 \mu\text{K}$ , and a  $\pm 5.5\%$  flux calibration uncertainty. The uncertainties in the centroid parameters  $X_0$  and  $Y_0$  include a  $\pm 4''$  pointing uncertainty and are given in units of arcseconds on the sky.

<sup>b</sup> Central Comptonization,  $y_0$ , is a derived parameter; assuming an electron temperature of 13.9 keV from Govoni et al. (2004) and 10.6 keV from Zhang et al. (2006), an SZE observation frequency of 152 GHz, and  $T_{\text{CMB}} = 2.728$  K. It is provided to facilitate comparisons with data at other wavelengths.

bolometer noise is stationary for each 100 s scan, the timestream noise is uncorrelated from scan to scan, and the map coverage is uniform. Our map coverage is not actually uniform, but we find through simulations of nonuniform Gaussian noise maps that the  $\chi^2$  statistic is not significantly affected. In addition, the validity of the approach is tested by inserting simulated clusters into the real timestream data; the simulated cluster parameters are accurately recovered within the estimated uncertainties.

Results of the  $\beta$  model parameter estimation are given in Table 2. Due to the degeneracy between the core radius  $\theta_c$  and  $\beta$  parameters, we assume a prior probability density on  $\beta$  of  $1.04^{+0.16}_{-0.10}$ , which is found from fits to *ROSAT* X-ray data by Ota & Mitsuda (2004). Hallman et al. (2007) find that in hydro/ $N$ -body simulations,  $\beta$  derived from fits to SZE profiles is higher than that from X-ray, with  $\beta_{\text{SZ}}/\beta_{\text{X-ray}} = 1.21 \pm 0.13$  for fits within  $r_{500}$ . We do not account for that factor here due to the significant uncertainty in the X-ray-derived  $\beta$  value, but we note that our SZE data prefer a higher value for  $\beta$  than the peak value of the prior. We further discuss this choice of prior in Section 5.5.

The best-fit  $\beta$  model fits the data well, with a reduced  $\chi^2$  value of 1.008, and with 7219 degrees of freedom (dof) has a probability to exceed (PTE) of 31.5%. The difference map between the data map,  $\mathcal{M}$ , and the best-fit filtered  $\beta$  model,  $\mathcal{B}'$ , shows no evidence of residual cluster structure or point sources.

Radial profile plots of the best-fit  $\beta$  model,  $\mathcal{B}$ , and the filtered  $\beta$  model map,  $\mathcal{B}'$ , are shown in Figure 4. Also plotted for comparison are the radially binned data from the unsmoothed non-source-masked map  $\mathcal{M}$ , used for model fitting, and the unsmoothed source-masked map, used to visualize extended emission (without the  $1'$  Gaussian smoothing used in Figures 2 and 3). Uncertainties in both sets of radially binned data are highly correlated due to large-spatial-scale correlated noise in the maps. The coincidence of the non-source-masked data ( $\mathcal{M}$ , filled circles) and the filtered best-fit  $\beta$  model ( $\mathcal{B}'$ , red solid line) show that the data and best-fit  $\beta$  model are in good agreement. The source-masked map preserves signal on larger spatial scales than the non-source-masked map, and is useful for visualizing extended emission on larger spatial scales. But, as expected, even the source-masked map attenuates signal on scales exceeding the  $4.75$  radius of the source masking, and thus has a lower signal amplitude when compared with the unfiltered  $\beta$  model ( $\mathcal{B}$ , blue-dashed line).

### 5.3. Radio and IR Source Contributions

Radio sources associated with a galaxy cluster and background IR galaxy sources can have a significant impact on the measurement of the SZE emission at 150 GHz. We interpret the published results of observations of the Bullet cluster at other frequencies and conclude that the measured SZE decrement is not significantly contaminated.

The most important source of potential confusion is a bright, dust obscured, lensed galaxy in the direction of the Bullet cluster recently reported by Wilson et al. (2008). This source has a flux density of  $13.5 \pm 0.5$  mJy at an observing frequency of 270 GHz, and is centered at R.A. 06<sup>h</sup>58<sup>m</sup>37<sup>s</sup>.31, decl.  $-55^\circ 57' 1''.5$  (J2000),  $\approx 56''$  to the east of the measured SZE centroid position, see Figure 3. Assuming a spectral index  $\alpha = 3$ , where  $S \propto \nu^\alpha$ , we expect a flux density of 1.94 mJy at 150 GHz corresponding to a temperature increment of  $\Delta T = 38 \mu\text{K}_{\text{CMB}}$  in the  $1.5$  arcmin<sup>2</sup> APEX-SZ beam solid angle. This lensed source is expected to be the dominant contribution to positive flux in the direction of the cluster, and we have repeated the  $\beta$  model fit taking it into account. We first add the source at its measured position with the predicted 150 GHz flux to the SZE  $\beta$  model and repeat the model fit. As expected, including the point source results in a slightly ( $\sim \sigma/3$ ) deeper decrement, however, the  $\chi^2$  of the model fit slightly increases. We next allow the flux of the point source to vary along with the other model parameters and find that values of positive flux are a poorer fit than no source at all. Therefore, we have no evidence for significant emission from this source at 150 GHz. For the results in this paper, we use cluster model parameters derived from fits that do not include this IR source.

The Bullet cluster is also associated with a number of relatively compact radio sources and one of the brightest cluster radio halos yet discovered. However, these sources are predicted to produce negligible temperature increments in the APEX-SZ beam when extrapolated to 150 GHz.

Liang et al. (2000) report the detection of eight radio point sources all of which have steeply falling spectra. Only two of these sources were detected with ACTA at 8.8 GHz, and they were found to have flux densities of  $3.2 \pm 0.5$  mJy and  $3.3 \pm 0.5$  mJy. The spectra of these sources, measured between 4.9 and 8.8 GHz are falling with  $\alpha = -0.93$  and  $\alpha = -1.33$ , respectively. Extrapolating to 150 GHz, the flux of these sources

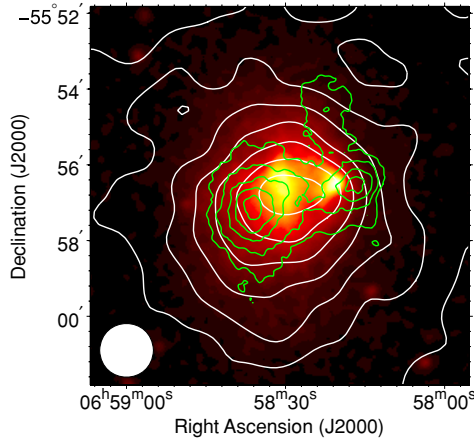


**Figure 5.** SZE map of the Bullet system from this work, in white contours, overlaid on an X-ray map from *XMM* observations. The green contours show the weak-lensing surface mass density reconstruction from Clowe et al. (2006). The SZE contour interval is  $100 \mu\text{K}_{\text{CMB}}$ .

(A color version of this figure is available in the online journal.)

are expected to be 0.24 and 0.07 mJy, corresponding to CMB temperature increments of  $\Delta T = 4.7$  and  $1.4 \mu\text{K}_{\text{CMB}}$  in the  $1.5 \text{ arcmin}^2$  APEX-SZ beam solid angle.

The radio halo in the Bullet cluster is very luminous, but has a characteristically steeply falling spectrum. Liang et al. (2000) measure the flux and spectra for the two main spatial components of the halo. At 8.8 GHz, they find the two components to have fluxes of 3.5 and 0.55 mJy, with spectral indices of  $\alpha = -1.3$  and  $\alpha = -1.4$ , respectively. Extrapolating to 150 GHz, the combined flux from the radio halo is expected to be  $\sim 0.1$  mJy. This emission is spread over an area comparable to the size of the cluster and therefore corresponds to a temperature increment  $< 1 \mu\text{K}_{\text{CMB}}$  in the APEX-SZ beam.

#### 5.4. Comparison with X-Ray Data

X-ray emission in the ionized intracluster gas is dominated by thermal bremsstrahlung. The X-ray surface brightness can be written as

$$S_X = \frac{1}{4\pi(1+z)^4} \int n_e n_i \Lambda_{ei} dl, \quad (6)$$

where  $n_{e,i}$  are the electron and ion densities in this gas,  $\Lambda_{ei}$  is the X-ray cooling function, and the integral is taken along the line of sight. The X-ray flux is proportional to the line-of-sight integral of the square of the electron density, resulting in emission that is more sensitive to local density concentrations than the SZE emission.

The Bullet subcluster and the bow shock are apparent in the X-ray surface brightness map shown in Figure 5. The SZE contour map of the Bullet cluster in Figures 2 and 3 is overlaid on an X-ray map and weak-lensing surface mass density reconstruction from Clowe et al. (2006).<sup>12</sup> The X-ray map is made from *XMM* data (observation Id: 0112980201) extracted in the (0.5–2) keV band, corresponding to Bullet rest-frame energies where the X-ray cooling function for hot gas is relatively insensitive to temperature. The map is smoothed with a  $12''$  Gaussian kernel.

The SZE contours do not resolve the subcluster. However, an elongation of the inner contours to the west suggests that a contribution from it may be detected. The observed SZE map is consistent with expectations; given the  $85''$  resolution of the SZE map, the different dependence of the X-ray and SZE signals on gas density, and the mass and temperature difference between the two merging components which predict a factor of  $\sim 10$  lower integrated pressure from the subcluster. There is no evidence in the SZE contours of a contribution from the lensed submillimeter bright galaxy discussed in Section 5.3.

#### 5.5. Mass-weighted Temperature

The combination of cluster SZE and X-ray measurements can be used to place constraints on the thermal structure of the intracluster gas. The SZE intensity is proportional to the product of the electron density and the electron temperature along the line of sight, see Equation (4). Therefore, if the electron density is known from another measurement, the SZE can be used to measure a mass-weighted temperature. For simplicity, we assume here that the intracluster gas is isothermal, but a more detailed comparison of the SZE surface brightness and projected density could be used to constrain the thermal structure in the cluster.

We perform this calculation with two different descriptions of the intracluster gas density. First, we model the spatial distribution of the intracluster gas as a spherical  $\beta$  model following Equation (1). We use  $\beta$  model parameters from Ota & Mitsuda (2004), derived from *ROSAT* HRI ( $\sim 2''$  resolution) measurements of the inner  $6'$  radius of the Bullet cluster:  $\beta = 1.04^{+0.16}_{-0.10}$ ,  $\theta_c = 112''.5^{+15.6}_{-10.4}$ , and  $n_{e0} = 7.2^{+0.3}_{-0.3} \times 10^{-3} \text{ cm}^{-3}$ .

We construct an X-ray-derived SZE surface brightness model from the  $\beta$  model electron surface density profile using Equation (4). To account for  $\beta$  model uncertainties, we incorporate the values and uncertainties for  $\beta$ ,  $\theta_c$ , and  $n_{e0}$  as independent Gaussian priors. We then use the analysis method described in Section 5.2 to minimize  $\chi^2$  on the difference between the X-ray-derived SZE model, convolved with the point-source transfer function, and the APEX-SZ non-source-masked data. The free parameters in the fit are the three  $\beta$  model parameters, the mass-weighted electron temperature  $T_{\text{mg}}$ , and the relative map alignment in R.A. and decl.

We find  $T_{\text{mg}} = 11.4 \pm 1.4 \text{ keV}$  after marginalizing over the other parameters in the fit and including the SZE flux calibration uncertainty and the effect of the APEX-SZ band center frequency uncertainty on the relativistic SZE spectrum  $f(x, T_{\text{mg}})$ . The reduced  $\chi^2$  of the best-fit model is 1.008 with an associated PTE of 31.3%, indicating that the spherical  $\beta$  density model and the assumption of isothermality produce an acceptable fit to the data.

Given the complex morphology of this merging system, the validity of the spherical  $\beta$  model is questionable. We therefore repeat the determination of the mass-weighted temperature by directly comparing X-ray measurements of the projected intracluster gas density with the measured SZE signal in order to produce a less model-dependent measurement of the mass-weighted temperature. We make use of the publicly available<sup>13</sup> electron surface density map derived from *Chandra* X-ray satellite data presented in Clowe et al. (2006). Using the same analysis as above, and marginalizing over the relative map alignment parameters, we find mass-weighted electron temperature  $T_{\text{mg}} = 10.8 \pm 0.9 \text{ keV}$ . The fit to the data is again

<sup>12</sup> Data are publicly available at <http://flamingos.astro.ufl.edu/1e0657/public.html>.

<sup>13</sup> <http://flamingos.astro.ufl.edu/1e0657/public.html>



**Table 3**  
Mass Estimates for the Bullet Cluster System

$T_e$ (keV) <sup>a</sup>	Mean Overdensity	$r_{\text{int}}$ (') <sup>b</sup>	$r_{\text{int}}$ (Mpc) <sup>c</sup>	Gas Mass Fraction	Gas Mass ( $10^{14} M_\odot$ )	Total Mass ( $10^{14} M_\odot$ )
$13.9 \pm 0.7$	$2506 \pm 233$	2.77	0.739	$0.124 \pm 0.022$	$0.944 \pm 0.105$	$7.56 \pm 0.70$
$13.9 \pm 0.7$	$961 \pm 98$	5.32	1.42	$0.106 \pm 0.024$	$2.20 \pm 0.33$	$20.6 \pm 2.1$
$10.6 \pm 0.2$	$2521 \pm 230$	2.15	0.572	$0.216 \pm 0.031$	$0.765 \pm 0.072$	$3.54 \pm 0.32$
$10.6 \pm 0.2$	$734 \pm 66$	5.32	1.42	$0.179 \pm 0.036$	$2.83 \pm 0.40$	$15.7 \pm 1.4$

**Notes.** Two different isothermal electron temperatures are assumed, in order to bracket the range of X-ray spectroscopic temperatures reported in the literature. The top two rows assume an isothermal electron temperature of  $13.9 \pm 0.7$  keV. The bottom two rows assume an isothermal electron temperature of  $10.6 \pm 0.2$  keV. For each electron temperature, we integrate to  $r_{2500}$ , the radius within which the mean cluster density is 2500 times greater than the critical density at the redshift of the cluster. For each electron temperature, we also integrate to a fixed radius of 1.42 Mpc, allowing a direct comparison to results in Zhang et al. (2006). This radius is also near where our measured SZE radial profile has unity signal-to-noise. For all results, we assume a  $\Lambda$ CDM cosmology, with  $h = 0.7$ ,  $\Omega_m = 0.27$ , and  $\Omega_\Lambda = 0.73$ . Uncertainties in the gas mass and gas mass fraction include a  $\pm 5.5\%$  SZE flux calibration uncertainty.

<sup>a</sup> Isothermal electron temperature.

<sup>b</sup> Angular integration radius.

<sup>c</sup> Physical integration radius.

good, with a reduced  $\chi^2 = 1.037$  and a PTE of 20.6%. This is in excellent agreement with the value  $T_{\text{mg}} = 11.4 \pm 1.4$  keV found from the above  $\beta$  model analysis.

Given the complex dynamics in the Bullet cluster, there have been several studies of the temperature structure (e.g., Finoguenov et al. 2005; Markevitch 2006; Andersson et al. 2007). There have also been several published results for the spectroscopic temperature within annuli about the cluster center. *Chandra* data were used by Govoni et al. (2004) to determine a spectroscopic X-ray temperature of  $T_{\text{spec}} = 13.9 \pm 0.7$  keV within 0.75 Mpc of the cluster center. From the analysis of *XMM* data within an annulus of 0.14–0.7 Mpc radius, Zhang et al. (2006) find a temperature of  $T_{\text{spec}} = 10.6 \pm 0.2$  keV. Analyzing the combination of *XMM* and *RXTE* data, Petrosian et al. (2006) find  $T_{\text{spec}} = 12.1 \pm 0.2$  keV within a radius of 0.95 Mpc. The published X-ray spectroscopic temperatures span a range much larger than the stated uncertainties in the measurements. Given the complex thermal structure for the cluster, and the presence of gas at temperatures corresponding to energies at or above the upper limits of the *Chandra* and *XMM* energy response, the variation in the measured X-ray spectroscopic temperature is not surprising. The mass-weighted temperature found with APEX-SZ falls near the lowest of the reported X-ray spectroscopic temperatures. However, we do not expect exact agreement between the mass-weighted and spectroscopic temperatures. Using *Chandra* data for a sample of 13 relaxed clusters, Vikhlinin et al. (2006) find that, due to the presence of thermal structure in the intracluster gas, the X-ray spectroscopic temperature is typically a factor of  $T_{\text{spec}}/T_{\text{mg}} = 1.11 \pm 0.06$  larger than the X-ray-derived mass-weighted electron temperature. This is consistent with the simulation results of Nagai et al. (2007) who find  $T_{\text{spec}}/T_{\text{mg}} \approx 1.14$  for relaxed clusters and  $T_{\text{spec}}/T_{\text{mg}} \approx 1.12$ , with a somewhat larger scatter, for unrelaxed systems. Naively applying this correction to the published X-ray spectroscopic temperatures, we infer results for mass-weighted temperatures that bracket the APEX-SZ result.

### 5.6. Gas Mass Fraction

Using the SZE measurements, we construct a model for the intracluster gas distribution which, when combined with X-ray measurements, can be used to determine the gas mass, total mass, and therefore gas mass fraction of the cluster. The gas mass is estimated by integrating a spheroidal model for the cluster gas, following LaRoque et al. (2006).

Several assumptions about the model must be made to estimate the gas mass. We assume that the cluster gas is isothermal in order to convert pressure to density. We also assume spheroidal symmetry for the gas distribution in order to convert the two-dimensional SZE integrated pressure measurement to a three-dimensional gas distribution.

We consider two simple cases, an oblate spheroid generated by rotation about the minor axis and a prolate spheroid generated by rotation about the major axis, where the symmetry axis is in the sky plane. The gas mass, under these assumptions, becomes

$$M_{\text{gas}}(r) = 8\mu_e n_{e0} m_p D_A^3 \int_0^{r/D_A} dX dY dZ \left( 1 + \left( \frac{X}{\theta_c} \right)^2 + \left( \frac{Y}{\eta\theta_c} \right)^2 + \left( \frac{Z}{\zeta\theta_c} \right)^2 \right)^{-3\beta/2}, \quad (7)$$

where  $\mu_e$  is the nucleon/electron ratio, taken to be 1.16 (Grego et al. 2001). The factor of 8 is due to integrating over only one octant of the spheroid. The factor  $\zeta$  is set to unity in the case of oblate spheroidal symmetry, while in the case of prolate spheroidal symmetry,  $\zeta$  is set to  $\eta$ .

The total cluster mass is estimated by assuming hydrostatic equilibrium and integrating the inferred gas distribution (Grego et al. 2000) to find

$$\rho_{\text{total}} = -\frac{kT_e}{4\pi G\mu m_p} \nabla^2 \ln \rho_{\text{gas}}. \quad (8)$$

Here,  $\mu$  is the mean molecular weight of the intracluster gas, which is assumed to be 0.62 (Zhang et al. 2006). Using Equations (7) and (8), and our model parameters in Table 2, we calculate the gas mass, total mass, and gas mass fraction for the cluster. In Table 3, we give these results. The gas mass fraction results for a prolate gas distribution model are  $\sim 3\%$  larger than those for an oblate model, while the total mass and gas mass are  $\lesssim 18\%$  larger. We quote only the oblate spheroidal results.

We calculate our results within two different radii. The first is the radius of the cluster at which its mean density is equal to 2500 times the critical density at the redshift of the cluster,  $r_{2500}$ . The second radius is 1.42 Mpc, which is the same radius used by Zhang et al. (2006) for their gas mass fraction calculation. This will allow for a more direct comparison to their result, and is also near where our measured SZE radial profile has unity signal-to-noise. For all results, we assume a  $\Lambda$ CDM cosmology,

with  $h = 0.7$ ,  $\Omega_m = 0.27$ , and  $\Omega_\Lambda = 0.73$ . The results of this analysis are summarized in Table 3. Under the assumption of a 10.6 keV mass-weighted temperature (the lowest of the published X-ray spectroscopic temperatures and near our mass-weighted temperature results in Section 5.5), we find gas mass fractions  $f_g = 0.216 \pm 0.031$  and  $0.179 \pm 0.036$  within  $r_{2500}$  and 1.42 Mpc, respectively. The fact that the computed gas fraction in the central region significantly exceeds the cosmic average determined by *WMAP5* ( $f_g = 0.165 \pm 0.009$ ; Dunkley et al. 2009), and a lower value observed in relaxed clusters ( $f_g \simeq 0.12$ ; see, e.g., Vikhlinin et al. 2009) is likely due to deviations of the intracluster gas from isothermal hydrostatic equilibrium. On larger scales, baryon fractions produced for the range of reported X-ray temperatures bracket the published results using X-ray and weak-lensing data. Bradač et al. (2006) measure a gas mass fraction  $f_g = 0.14 \pm 0.03$  by comparing the gas mass calculated from *Chandra* X-ray measurements to weak-lensing total mass measurements in a  $4.9 \times 3.2$  box roughly centered around the cluster. Zhang et al. (2006) measured a gas mass fraction  $f_g = 0.161 \pm 0.018$  within a radius of 1.42 Mpc. Despite the limitations of applying a hydrostatic equilibrium model to this merging cluster, the APEX-SZ results for the gas mass fraction are in good agreement with previous work.

## 6. CONCLUSIONS

Measurements of the SZE provide a robust and independent probe of the intracluster gas properties in galaxy clusters. The APEX-SZ 150 GHz observations detect the Bullet system with  $23\sigma$  significance within the central  $1'$  radius of the SZE centroid position. We do not expect to see a resolved signal from the Bullet subcluster in the 150 GHz  $85''$  FWHM resolution SZE maps, and no obvious feature, such as a secondary peak, is present. We expect no significant contamination of the observed SZE decrement due to radio sources, and there is no evidence for significant contamination by a known bright-lensed dusty galaxy.

We process an elliptical  $\beta$  model through the observation transfer function and fit it to the measured temperature decrement map. We also measure the cluster mass-weighted electron temperature and gas mass fraction with the SZE data. Combining the APEX-SZ map with a map of projected electron surface density from *Chandra* X-ray observations, we determine the mass-weighted temperature of the cluster gas to be  $T_{\text{mg}} = 10.8 \pm 0.9$  keV. This value is consistent with the lowest X-ray spectroscopic temperatures reported for this cluster and should be less sensitive to the details of the cluster thermal structure. The derived baryon fraction is also found to be in reasonable agreement with previous X-ray and weak-lensing determinations.

Throughout this work, we make an assumption of isothermal cluster gas. Clearly, incorporating thermal structure, measured by X-ray observations, in the analysis of the SZE data would improve the determination of the gas distribution and gas mass fraction. Ultimately, a more sophisticated analysis could be implemented that combines X-ray, SZE, and weak-lensing data and relaxes assumptions of hydrostatic equilibrium between the gas and dark matter components of the cluster. This is particularly important for a detailed understanding of actively merging systems such as the Bullet cluster.

We thank the staff at the APEX telescope site, led by David Rabanus and previously by Lars-Åke Nyman, for their dedicated and exceptional support. We also thank LBNL engineers John

Joseph and Chinh Vu for their work on the readout electronics. APEX-SZ is funded by the National Science Foundation under grants AST-0138348 and AST-0709497. Work at LBNL is supported by the Director, Office of Science, Office of High Energy and Nuclear Physics, of the U.S. Department of Energy under contract no. DE-AC02-05CH11231. Work at McGill is supported by the Natural Sciences and Engineering Research Council of Canada and the Canadian Institute for Advanced Research. R.K. acknowledges partial financial support from MPG Berkeley-Munich fund. N.W.H. acknowledges support from an Alfred P. Sloan Research Fellowship.

## REFERENCES

- Andersson, K., Peterson, J. R., & Madejski, G. 2007, *ApJ*, **670**, 1010  
 Andreani, P., et al. 1999, *ApJ*, **513**, 23  
 Benson, B. A., et al. 2003, *ApJ*, **592**, 674  
 Birkinshaw, M. 1999, *Phys. Rep.*, **310**, 97  
 Bradač, M., et al. 2006, *ApJ*, **652**, 937  
 Cavaliere, A., & Fusco-Femiano, R. 1978, *A&A*, **70**, 677  
 Chamberlain, R. A., & Bally, J. 1995, *Int. J. Infrared Millim. Waves*, **16**, 907  
 Clowe, D., Bradač, M., Gonzalez, A. H., Markevitch, M., Randall, S. W., Jones, C., & Zaritsky, D. 2006, *ApJ*, **648**, L109  
 Dobbs, M., et al. 2006, *New Astron. Rev.*, **50**, 960  
 Dunkley, J., et al. 2009, *ApJS*, **180**, 306  
 Finoguenov, A., Böhringer, H., & Zhang, Y.-Y. 2005, *A&A*, **442**, 827  
 Gomez, P., et al. 2004, in AIP Conf. Proc. 703, *Plasmas in the Laboratory and in the Universe: New Insights and New Challenges*, ed. G. Bertin, D. Farina, & R. Pozzoli (Melville, NY: AIP), 361  
 Govoni, F., Markevitch, M., Vikhlinin, A., VanSpeybroeck, L., Feretti, L., & Giovannini, G. 2004, *ApJ*, **605**, 695  
 Grego, L., Carlstrom, J. E., Joy, M. K., Reese, E. D., Holder, G. P., Patel, S., Cooray, A. R., & Holzapfel, W. L. 2000, *ApJ*, **539**, 39  
 Grego, L., Carlstrom, J. E., Reese, E. D., Holder, G. P., Holzapfel, W. L., Joy, M. K., Mohr, J. J., & Patel, S. 2001, *ApJ*, **552**, 2  
 Güsten, R., Nyman, L. Å., Schilke, P., Menten, K., Cesarsky, C., & Booth, R. 2006, *A&A*, **454**, L13  
 Hallman, E. J., Burns, J. O., Motl, P. M., & Norman, M. L. 2007, *ApJ*, **665**, 911  
 Hill, R. S., et al. 2009, *ApJS*, **180**, 246  
 LaRoque, S. J., Bonamente, M., Carlstrom, J. E., Joy, M. K., Nagai, D., Reese, E. D., & Dawson, K. S. 2006, *ApJ*, **652**, 917  
 Laurent, G. T., et al. 2005, *ApJ*, **623**, 742  
 Lee, A. T., Richards, P. L., Nam, S. W., Cabrera, B., & Irwin, K. D. 1996, *Appl. Phys. Lett.*, **69**, 1801  
 Liang, H., Hunstead, R. W., Birkinshaw, M., & Andreani, P. 2000, *ApJ*, **544**, 686  
 Markevitch, M. 2006, in *The X-Ray Universe 2005*, ed. A. Wilson (ESA SP-604; Noordwijk: ESA), 723  
 Muhleman, D. O., & Berge, G. L. 1991, *Icarus*, **92**, 263  
 Nagai, D., Vikhlinin, A., & Kravtsov, A. V. 2007, *ApJ*, **655**, 98  
 Nolte, M. R., et al. 2009, *ApJS*, **180**, 296  
 Nozawa, S., Itoh, N., Kawana, Y., & Kohyama, Y. 2000, *ApJ*, **536**, 31  
 Ota, N., & Mitsuda, K. 2004, *A&A*, **428**, 757  
 Peterson, J. B., Radford, S. J. E., Ade, P. A. R., Chamberlain, R. A., O'Kelly, M. J., Peterson, K. M., & Schartman, E. 2003, *PASP*, **115**, 383  
 Petrosian, V., Madejski, G., & Luli, K. 2006, *ApJ*, **652**, 948  
 Reese, E. D., et al. 2000, *ApJ*, **533**, 38  
 Richards, P. 1994, *J. Appl. Phys.*, **96**, 1  
 Rudy, D. J., Muhleman, D. O., Berge, G. L., Jakosky, B. M., & Christensen, P. R. 1987, *Icarus*, **71**, 159  
 Sayers, J. 2007, PhD thesis, California Institute of Technology  
 Sayers, J., et al. 2009, *ApJ*, **690**, 1597  
 Schwan, D., et al. 2003, *New Astron. Rev.*, **47**, 933  
 Scott, K. S., et al. 2008, *MNRAS*, **385**, 2225  
 Springel, V., & Farrar, G. R. 2007, *MNRAS*, **380**, 911  
 Sunyaev, R. A., & Zel'dovich, Y. B. 1970, *Comments Astrophys. Space Phys.*, **2**, 66  
 Vikhlinin, A., Kravtsov, A., Forman, W., Jones, C., Markevitch, M., Murray, S., & VanSpeybroeck, L. 2006, *ApJ*, **640**, 691  
 Vikhlinin, A., et al. 2009, *ApJ*, **692**, 1033  
 Wilson, G. W., et al. 2008, *MNRAS*, **390**, 1061  
 Wright, E. L. 1976, *ApJ*, **210**, 250  
 Wright, E. L. 2007, arXiv:astro-ph/0703640v1  
 Zhang, Y.-Y., Böhringer, H., Finoguenov, A., Ikebe, Y., Matsushita, K., Schuecker, P., Guzzo, L., & Collins, C. A. 2006, *A&A*, **456**, 55